



# Co-seismic and post-seismic deformation associated with the 2018 Lombok, Indonesia, earthquake sequence, inferred from InSAR and seismic data analysis

Siyuan Zhao<sup>\*</sup>, Simon McClusky, Phil R. Cummins, Meghan S. Miller

Research School of Earth Sciences, Australian National University, Canberra, ACT, Australia

## ARTICLE INFO

Edited by Jing M. Chen

### Keywords:

InSAR displacement  
Slip distribution  
Viscoelastic relaxation  
Aftershock clustering  
Earthquake sequence

## ABSTRACT

In 2018, four deadly (M<sub>w</sub> 6.2–6.9) earthquakes struck the north coast of Lombok Island on 28 July, 5 August, and 19 August. The slip distributions of the three mainshocks are modeled in this study by inverting the co-seismic deformation imaged using an interferometric analysis of Sentinel-1 synthetic aperture radar measurements (InSAR), based on rectangular dislocations embedded in a multi-layered elastic half-space. Our best-fit co-seismic slip model suggests the estimated maximum fault slips of 1.3 m, 2.2 m, and 2.5 m for the mainshocks from July to August, located at depths of 9.6 km, 13.6 km, and 22.2 km, respectively. We applied an unsupervised learning method (ST-DBSCAN) to cluster the relocated aftershocks so that we could identify the source of each aftershock. The clustered aftershocks are primarily distributed in the areas with increased Coulomb stress and are less abundant in the maximum slip patch on the three rupture faults, indicating consistency with our estimated co-seismic slip model. In addition, we use an InSAR time series, consisting of 337 descending and 177 ascending Sentinel-1 acquisitions to investigate the time-dependent, post-seismic deformation in the two years following the Lombok 2018 earthquake sequence, based on a pure afterslip model and a combined model that simulates viscoelastic relaxation and afterslip simultaneously. The best-fit combined model suggests a Maxwell viscosity of  $1 \times 10^{18}$  Pa s for both the lower crust and asthenosphere, and it reveals that the maximum of the cumulative afterslip within two years is  $\sim 0.7$  m, along the northwestward up-dip continuation of the co-seismic rupture area.

## 1. Introduction

The island of Lombok is located at the western edge of the Nusa Tenggara region of eastern Indonesia, which is tectonically bounded in the north by the southward-dipping Flores back-arc thrust fault and in the south by the northward-dipping Sunda subduction megathrust (Hamilton, 1979; Salman et al., 2020; Samsi et al., 2020; Fig. 1a). An active, 3726 m-high volcano, the Rinjani-Samalas volcanic complex (henceforth referred to simply as ‘Rinjani’, or ‘Rinjani volcano’), lies on Lombok approximately 300 km north of the Sunda trench (Foden, and JD, F., 1981; Fig. 1b). In July and August 2018, a series of four deadly (M<sub>w</sub> 6.2–6.9) shallow earthquakes (< 40 km depth) struck the northern region of Lombok, leading to about 590 deaths and nearly 90,000 heavily damaged buildings, according to the statistics from National Oceanic and Atmospheric Administration, see also Salman et al. (2020); Yang et al. (2020). The earthquake sequence occurred over a span of

three weeks, starting with an M<sub>w</sub> 6.4 event on 28th July (hereafter referred to as ‘28 J’) near the northern tip of Lombok. On 5th August, a larger M<sub>w</sub> 6.9 event occurred to the northwest of the island, around 10 km west of the 28 J epicentre (hereafter referred to as ‘5 A’). In the next two weeks, more than one thousand M<sub>w</sub> < 5 aftershocks occurred surrounding event 5 A, with the magnitude of the largest one reaching M<sub>w</sub> 5.9. Subsequently, two earthquakes of M<sub>w</sub> 6.2 and M<sub>w</sub> 6.9 happened on 19 August. Due to the close spatial and temporal proximity (only 4 km and 10 h apart) and similar earthquake focal mechanisms, the M<sub>w</sub> 6.2 earthquake is considered as a foreshock of the M<sub>w</sub> 6.9 event (Hanifa et al., 2019); in this study, we will treat these two earthquakes as a single event, hereafter referred to as ‘19 A’ (Salman et al., 2020; Samsi et al., 2020; Yang et al., 2020; Fig. 1b).

These earthquakes occurred along a series of faults with different strikes and dips that form part of the Flores back-arc thrust system, and appear to have failed in a series of cascading ruptures based on

<sup>\*</sup> Corresponding author.

E-mail address: [Siyuan.Zhao@anu.edu.au](mailto:Siyuan.Zhao@anu.edu.au) (S. Zhao).

<https://doi.org/10.1016/j.rse.2024.114063>

Received 19 June 2023; Received in revised form 7 February 2024; Accepted 16 February 2024

Available online 20 February 2024

0034-4257/© 2024 The Author(s). Published by Elsevier Inc. This is an open access article under the CC BY license (<http://creativecommons.org/licenses/by/4.0/>).

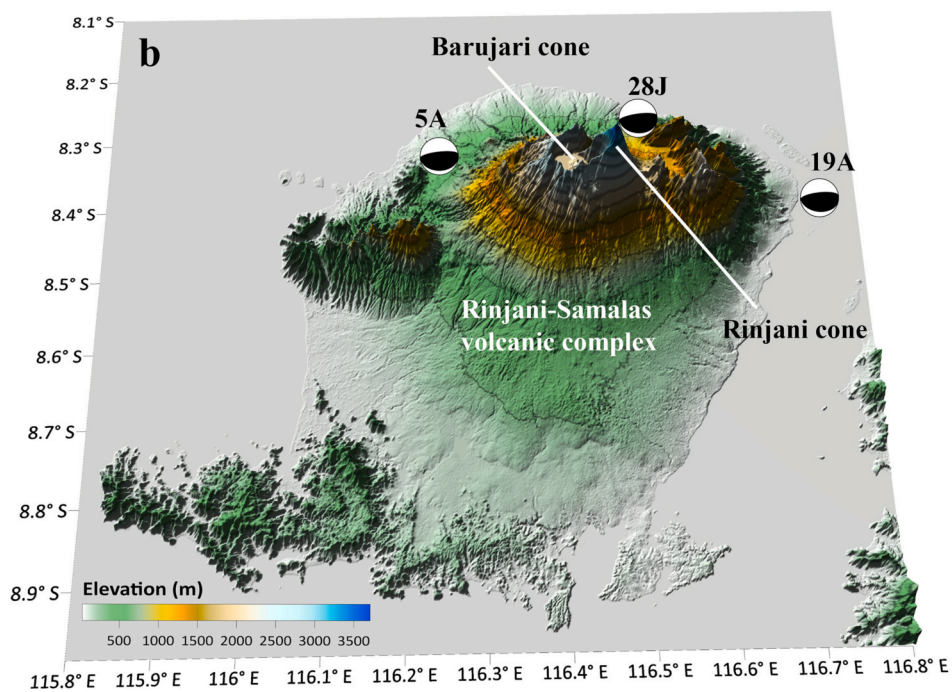
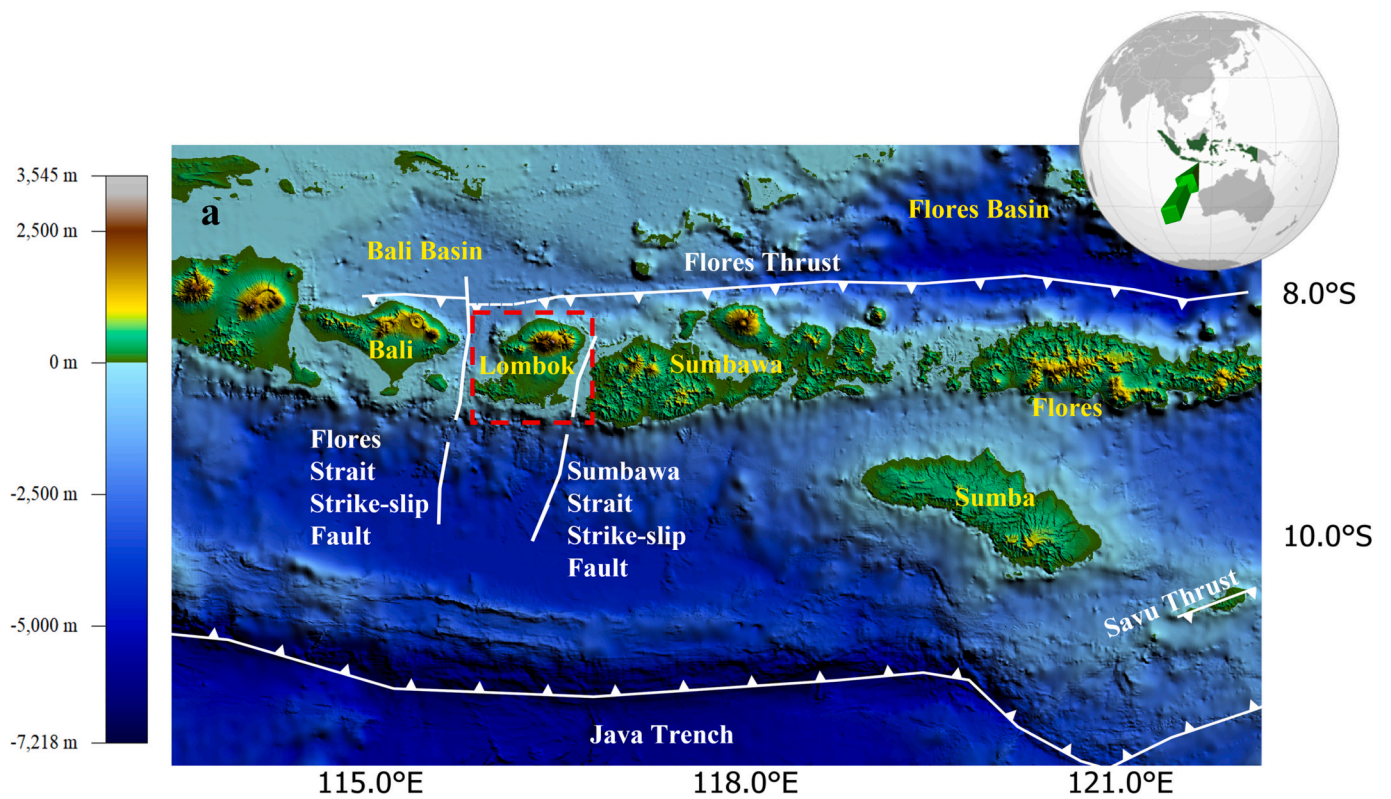


**Fig. 1.** a) The tectonic setting of the central Sunda-Banda arc region. The faults are derived from [Sasmi et al. \(2020\)](#). The white dashed line represents the extension of the West Flores thrust ([Silver et al., 1983](#)). b) The perspective view of Lombok Island (red rectangle in [Fig. 1a](#)) is based on the 3-arc-second Shuttle Radar Topography Mission (SRTM-3) digital elevation model (DEM). The earthquake focal mechanisms of the major earthquakes in the 2018 Lombok earthquake sequence from the Global Centroid Moment Tensor (GCMT) catalog are shown. (For interpretation of the references to colour in this figure legend, the reader is referred to the web version of this article.)

Interferometric Synthetic Aperture Radar (InSAR) and seismic data analysis (Salman et al., 2020; Wang et al., 2020; Yang et al., 2020). Wang et al. (2020) was the first geodetic-based study that quantified the characteristics of the fault rupture of the earthquake sequence by inverting a set of Sentinel-1 InSAR measurements. Following this study, several attempts based on the InSAR and/or seismic measurements have been made to analyze the mechanism causing the earthquake sequence and the rupture process on the faults. However, the inferred fault geometries and co-seismic slip distribution among these studies are variable (Lythgoe et al., 2021; Salman et al., 2020; Wang et al., 2020; Yang et al., 2020). One reason may be the quality of the dataset used in the inversion. The accuracy of InSAR-derived surface deformation is significantly influenced by the spatial-temporal variations of atmospheric water vapor, topography, and vegetation; different approaches chosen to deal with these effects will influence the estimated rupture model results, and the missing data in the offshore deformation field can lead to instability in inversion results (Yu et al., 2018). In addition, the single track (either descending or ascending) used in some studies (e.g., Wang et al. (2020) and Yang et al. (2020)) may be inadequate for characterizing surface deformation. The importance of combining multi-geometry InSAR datasets in such inversions has been emphasized in previous studies (Pritchard et al., 2002).

Supendi et al. (2020) relocated >60 aftershocks between the period of 28 J and 5 A; and 116 and 173 relocated aftershocks were identified for the period from 5 to 18 August 2018 and 19 August to 22 November 2018, respectively, using a teleseismic double-difference method. Sasmi et al. (2020) relocated 3259 aftershocks using data from 20 seismographs deployed on Lombok Island between 4 August to 9 September 2018. The location of the aftershocks aids in the identification of the rupture plane and the direction of the rupture propagation (Galović et al., 2009). Supendi et al. (2020) suggest that the 2018 Lombok earthquake sequence exhibited two different rupture behaviors: a westward propagated rupture in 5 A followed by an eastward propagated rupture in 19 A. However, the mainshocks of this earthquake sequence are close to each other spatially and temporally, resulting in aftershock sequences caused by different mainshocks that overlap in space and time. Separating these aftershock sequences is important for understanding how they relate to the mainshock rupture processes and stress propagation. Another factor that may be complicating our understanding of the earthquake sequence is the presence of the Rinjani volcano close to the faults. Salman et al. (2020) suggested that heat from Rinjani's volcanic activity inhibited down-dip propagation of rupture in the 5 A and 28 J events by elevating the base of the seismogenic zone by 8 km (Lythgoe et al., 2021).

Following a large earthquake, part of the co-seismic stress changes will be relieved by post-seismic deformation, via afterslip and viscoelastic relaxation. Exploration of these processes can help us better understand fault slip behavior, stress transfer and earth rheology (Sun and Wang, 2015). In this study, we perform a comprehensive analysis of relocated aftershocks, static Coulomb stress changes, and co-seismic and post-seismic deformation, to improve our understanding of the nature of rupture during the earthquake sequence. We combine the co-seismic InSAR measurements with the relocated aftershocks to investigate the seismogenic relationship between the mainshocks and the characteristics of the faults or fault system that controls where and how often these events occur. The co-seismic slip model estimated in most previous studies (e.g., Salman et al., 2020; Wang et al., 2020) was embedded in an elastic homogeneous half-space with uniform Poisson's ratio (Okada, 1985), which is a commonly used material property assumption. Here we propose to estimate the co-seismic slip distribution based on a multilayered elastic half-space derived from the Sasmi et al. (2020) 1D local seismic velocity (Wang et al., 2003). We then cluster the relocated aftershocks from Sasmi et al. (2020) and Supendi et al. (2020) using an unsupervised learning method, separating the identifiable aftershock sequences from the more diffuse earthquake activity. In the post-seismic deformation analysis, we considered the effect of viscosity because of

the proximity of Rinjani, which may be associated with elevated temperature and low viscosity in the lower crust (Lythgoe et al., 2021). We therefore model the viscoelastic relaxation and afterslip simultaneously based on the InSAR time series observations of the post-seismic surface deformation for as long as ~2 years after the earthquake sequence, which has not been considered in previous studies of the 2018 Lombok earthquake sequence. The static Coulomb stress changes have also been analyzed to explain the co/post-seismic behavior and the distribution of the aftershocks, and to evaluate the earthquake-volcano interactions.

## 2. Tectonic and geological features

The rupture propagation and cascading behavior of the 2018 Lombok earthquake sequence occurred in a complex tectonic setting that includes the Flores back-arc thrust and the Rinjani volcano (Lythgoe et al., 2021; Salman et al., 2020; Wang et al., 2020; Yang et al., 2020). Several different assumptions about the origin of the Flores back-arc thrust have been proposed, including the reversal of eastern Sunda arc subduction polarity (Hamilton, 1979; McCaffrey and Nábělek, 1984), stress propagation across the forearc driven by the continental collision (Silver et al., 1983) and gravitational sliding/spreading of the upper plate.

The nature of the Flores back-arc thrust, especially its western end north of Lombok, is still unclear. Hamilton (1979) suggested that the western zone of the Flores thrust should terminate north of central Lombok due to thrusting at the Bali basin and the intrusion of magmatic material overriding the collision between the Australian continent and the arc, i.e., arc-continental collision, which requires no external force or net shortening across the arc. Silver et al. (1983) suggested that the main driving mechanism of thrusting in the Bali basin is the arc-continental collision, based on seismic reflection and refraction, bathymetry, gravity and magnetics datasets. This tectonic interpretation has been the basis of kinematic studies that describe the Flores back-arc thrust as the northern boundary of the eastern Sunda-Banda arc zone, spanning over 2000 km with an estimated convergence rate of ~10 mm/yr at the Lombok segment (Zhao et al., 2023). In a recent marine seismic study (Yang et al., 2020), the Lombok-Bali segment of the Flores thrust does not rupture to the surface, i.e., blind thrust fault, deforming the seabed by folds rather than faults.

All previous studies of the 2018 Lombok earthquake sequence (e.g., Lythgoe et al., 2021; Salman et al., 2020; Wang et al., 2020) found that each mainshock ruptured a fault having a geometry (i.e., strike and dip) different from the other events, and the relationship between these faults and the Flores back-arc thrust is still unclear. Wang et al. (2020) and Yang et al. (2020) suggested that the source faults of the earthquake sequence were low-angle subparallel thrust fault, i.e., imbricate faults, associated with the main Flores back-arc thrust. However, in Lythgoe et al. (2021), the source faults were interpreted as different parts of the Flores back-arc thrust, with their varying geometries reflecting irregularities in the fault surface resulting from the thermal "squeezing" of the seismogenic zone caused by heat sourced from the active Rinjani volcano on Lombok.

## 3. Co-seismic deformation

### 3.1. InSAR data processing

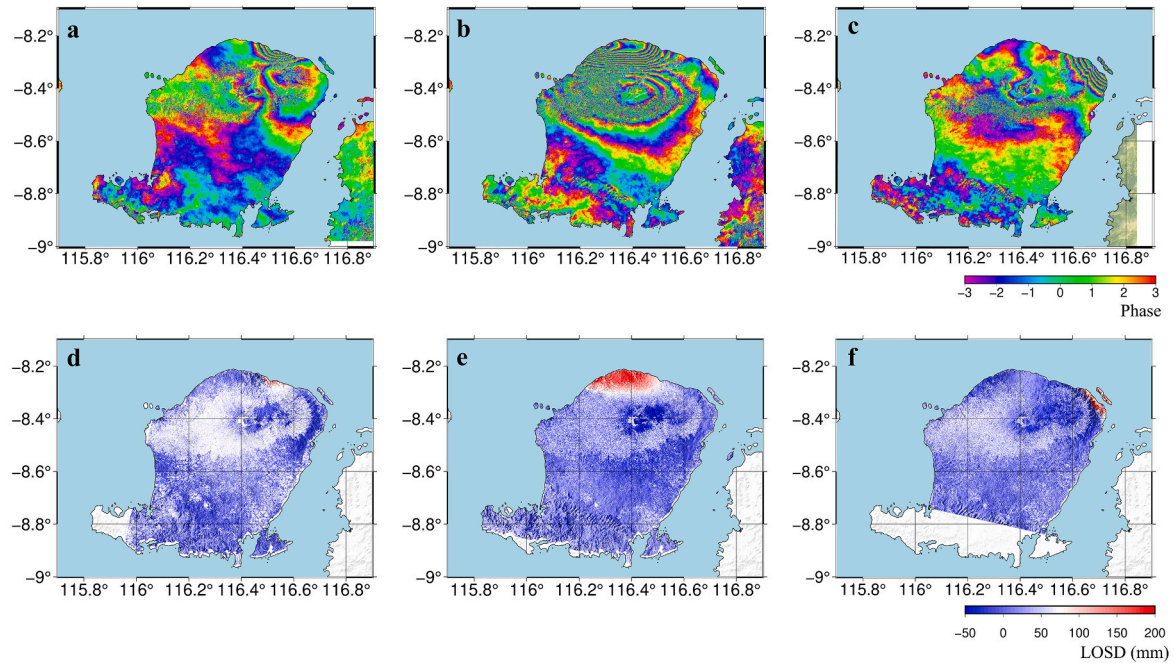
InSAR is a technique for measuring ground surface movement, which is based on the use of two SAR images of a region acquired by repeated acquisition at different times from which the relative phase delay for each radar pulse pixel is obtained (Gabriel et al., 1989). On volcanoes, such measurements are often used to infer the causative processes of deformation, e.g., fault movement or inflation/deflation of a magma chamber or conduit (Hanssen, 2001; Lin and Stein, 2004). To measure the co-seismic surface deformation caused by the 2018 Lombok earthquake sequence, we used the descending and ascending track data of

Sentinel-1 constellation. For each main event, the onshore area affected by earthquake rupture is covered by two pairs of selected SAR images, including both ascending and descending tracks (Table S1). We utilize the GMTSAR software (Sandwell et al., 2011) for InSAR processing with the Single Look Complex products. The SRTM-3 DEM and precise orbits are used to model and remove the topographic component. Then the interferogram is filtered by using an adaptive Goldstein filter to reduce the effects of phase noise and unwrapped. Before unwrapping the relative phase, we mask out the low-coherence and ocean pixels.

Due to the phase measurement's inherent 1-wavelength ambiguity, interferograms before unwrapping typically have a fringed appearance, as indicated in the "wrapped" interferograms in Fig. 2. Phase-unwrapping removes this ambiguity, resulting in maps of changes in Line-of-Sight (LOS) distance, i.e., displacement in the satellite to a ground direction (Fig. 2).

The SAR phase delay is affected by spatiotemporal variations in atmospheric temperature, pressure and water vapor (Yu et al., 2018), mainly due to the destabilization of the troposphere by vertical wind

### Descending



### Ascending

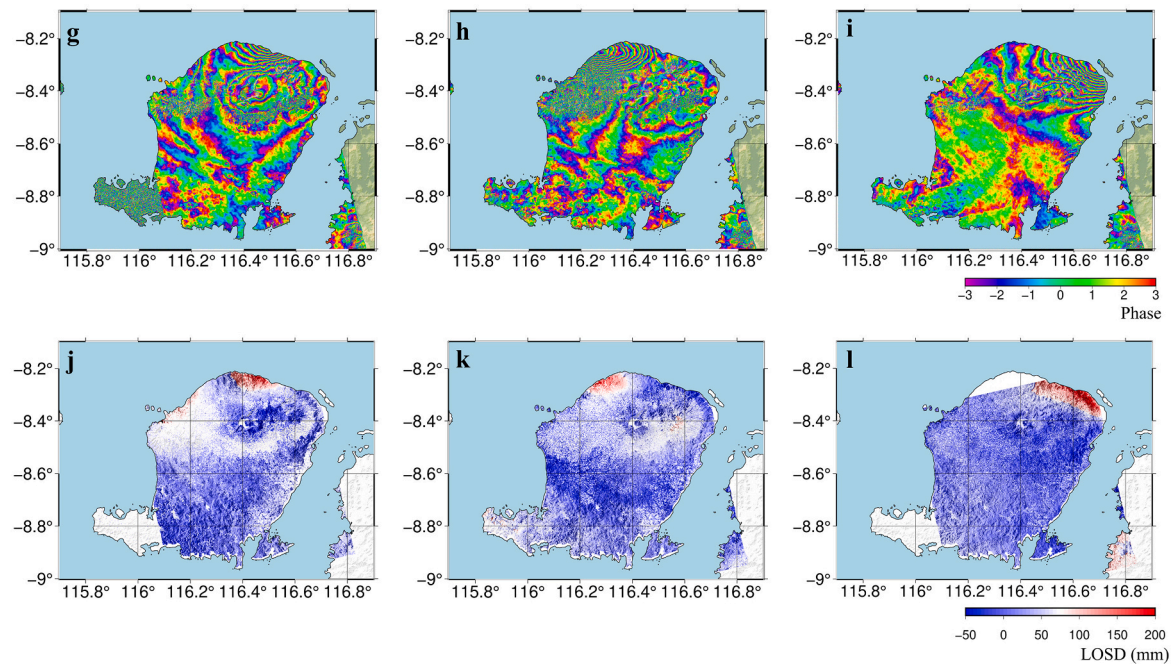


**Fig. 2.** The wrapped interferograms (a ~ c; g ~ i) and the corresponding unwrapped displacements which have been corrected atmospheric delay using GACOS (d ~ f; j ~ l) for 28 J, 5 A and 19 A respectively on both descending (upper panel) and ascending (lower panel) tracks.

shear near the surface and radiative heating (Hanssen, 2001). Albino et al. (2020) demonstrated the effectiveness of using high-resolution weather models to correct the atmospheric phase delay in tropical volcano regions like eastern Indonesia (in particular Agung volcano in Bali, 100 km west of Lombok). Therefore, we use the high-resolution tropospheric delay products of the Generic Atmospheric Correction Online Service (GACOS), to correct the unwrapped interferograms for atmospheric delays (Yu et al., 2018; Fig. S1). This atmospheric correction is important, since the maximum GACOS differential delay for the Lombok region during the co-seismic periods is  $\sim 14$  cm, similar to the level of ground motion that can be caused by urban subsidence and landslides (Yu et al., 2018; Fig. S1).

The wrapped and unwrapped interferograms of the 2018 Lombok earthquake sequence indicate that the ground deformation caused by the earthquake rupture was mainly concentrated on the northern coast of Lombok (Fig. 2). The wrapped interferograms of both descending and ascending tracks for the three events illustrate high-coherence fringe patterns near the northern coast, as well as a low-coherence signal distributed on the Rinjani edifice. Except for the caldera region, the slopes of Rinjani are covered by an evergreen broadleaf forest that impedes the Sentinel-1C-band wave from reaching the ground, and the noisy, low-coherence signals are mainly concentrated in these areas (Saputra et al., 2020; Fig. 2). For the 28 J event, four and six high-coherence fringes can be observed in the 28 J descending and ascending wrapped interferograms respectively, concentrated along the northeast coast of Lombok. After atmospheric correction, the unwrapped results suggest maximum LOS displacements of 14.8 cm and 20.0 cm, for descending and ascending paths, respectively, towards the satellite (Fig. 2). For event 5 A, the deformation is also concentrated near the north coast of Lombok, just west of the deformation zone of event 28 J. The LOS displacements for 5 A reach a maximum of 26.2 cm and 33.2 cm towards descending and ascending satellites, respectively. Both ascending and descending results are plagued by the loss of coherent signal around the west part of Rinjani. The ground movement for event 19 A is concentrated in the northeast of Lombok Island, with maximum positive LOS displacements of 23.6 cm and 24.4 cm (descending and ascending, respectively).

For computational efficiency in the inversion of the InSAR data, we down-sampled the interferograms to a hundred-thousand-pixel level using the adaptive quadtree (gradient-based) sub-sampling method, which down-samples less in areas with high gradients of displacement and vice versa (Jónsson et al., 2002). Compared with uniform sub-sampling (Pritchard et al., 2002), which is most suitable in situations where the deformation is relatively uniform, and resolution-based sub-sampling (Lohman and Simons, 2005) that needs the fault geometries as the prerequisites, the quadtree down-sampling approach is more suitable for this 2018 Lombok earthquake sequence. This is because the deformation associated with each earthquake is characterized by highly localized, irregularly spaced deformation with little known prior information about the geometric parameters of the deformation source (Jónsson et al., 2002).

However, the quadtree algorithm will oversample the areas where higher displacement gradients are caused by spatially correlated noise (e.g., tropospheric delay, topographic residuals), and also the random noise caused by phase decorrelation and unwrapping errors, leading to inaccurate estimates. Usually, the threshold that controls the phase variance can be adjusted to increase the down-sampling in nondeforming areas (Bagnardi and Hooper, 2018). However, on Lombok, the evergreen broadleaf forests surrounding the volcano result in short wavelength, decorrelated noise, which swamps the deformation signal and leads to the oversampling of the high-noise areas (Saputra et al., 2020; Fig. S2). Therefore, even though the down-sampling in the noisy area increased with an increased quadtree threshold value, the down-sampling of the deformation area increased as well (Fig. S2). In this study, rather than increasing the threshold value, the noise was manually removed to preserve more high-quality deformation sample points.

After down-sampling in areas that were affected by high noise, the high gradient noise is then easily identified (Fig. S2). Compared with previous studies that removed all the pixels located at the noisy Rinjani volcano region (e.g., Wang et al., 2020) or that down-sampled the unwrapped interferograms by only adjusting the quadtree threshold (e.g., Salman et al., 2020), our results maintain the deformation signals surrounding the volcano and avoid down-sampling in regions with large but well-resolved deformation gradients (Fig. S2).

### 3.2. Co-seismic slip modeling

#### 3.2.1. Fault geometry and uniform slip modeling

In this study, the descending and ascending interferograms were inverted simultaneously by using the Geodetic Bayesian Inversion Software (GBIS) to estimate the fault geometry assuming uniform slip (Bagnardi and Hooper, 2018). GBIS is based on the Bayesian probabilistic inversion algorithm, which is capable of inverting multiple independent data sets. GBIS uses the Okada (1985) model for dislocation in an elastic, homogeneous half-space as the forward model for dipping faults with a uniform slip (Bagnardi and Hooper, 2018). Cattin et al. (1999) found that, for a dip-slip dislocation on a planar rectangular fault, the use of a uniform instead of a more realistic layered half-space may result in discrepancies in the co-seismic displacement of up to 40%, but this difference is mainly in the horizontal displacement near the fault. The effect of layering on the estimation of fault orientation using InSAR, which is mainly sensitive to vertical displacement, is likely to be much less. Cattin et al. (1999) suggested that the estimated dip is insensitive to layering. Fault strike is determined from the azimuthal variation of displacement, which will be similar for both uniform and layered models since both are azimuthally symmetric.

The results of Bayesian inversion for the fault geometry parameters and their corresponding uncertainties are shown in Tables S2 and S3. Our uniform slip model includes three south-dipping seismogenic fault planes with significant variations in strike and dip that closely match the variations in fault geometry estimated by Salman et al. (2020) which was obtained using inversion of seismic waveforms using a layered seismic velocity structure, but differ more significantly from the InSAR-derived results of Wang et al. (2020) which used a uniform elastic half-space (Table S4). We believe the difference in our fault orientation results with respect to Wang et al. (2020) stems from our use of both descending and ascending orbit data, which is better able to resolve the true displacement, especially where the topography is complex (Smitarello et al., 2019). As demonstrated in Fig. S3, the descending and ascending LOS displacement for the three mainshocks have been well-modeled in the coastal region, with residuals randomly distributed in most of the estimated geometries. Since the model is based on a simple rectangular fault with uniform slip, there may be some variation in displacement that is poorly modeled due to the spatial variations in slip over the fault plane, which we consider below.

#### 3.2.2. Slip distribution modeling

After estimating the source fault geometry using GBIS, we extended the length and width of the fault plane and divided it into a  $2 \text{ km} \times 2 \text{ km}$  grid to detect the distribution of the slip along the fault plane using the Steepest Descent Method (SDM; Wang et al., 2013), which is a first-order iterative algorithm for constrained least-squares optimization. This method has been widely used in many different studies that have successfully applied it to the inversion of co-seismic slip and afterslip (e.g., Diao et al., 2014; Liu et al., 2016). In this study, we used a nine-layer 1D velocity model derived from Samsi et al. (2020; Table S5). The influence of the topographic surface on inferred slip models was accounted for by using the receiver elevation correction method (Williams and Wadge, 1998). During the inversion, the descending and ascending interferograms were weighted by their respective reference misfits as described in the dataset (Smitarello et al., 2019). In order to obtain the uncertainty of the estimate slip distribution, we performed the SDM

inversion 100 times, with the input data for each inversion comprised of the observational LOS displacement and random noise based on the Variance-Covariance Matrix (VCM) method (Hanssen, 2001). The model uncertainties are reflected in the standard deviation of the 100 sets of the slip distribution results (Hong et al., 2018; Fig. S4).

The modeled InSAR displacement values provide a good fit to the observations, which indicates that the layered earth model and distributed slip can well explain the source dislocation (Fig. 3). Table S4 compares the parameters of the earthquake sequence derived from our best-fit InSAR model with that of the previous studies and different institutes. The centroid depth for the earthquakes estimated in this study is where the maximum slip displacement is located, indicating the center of energy release. Our distributed slip models suggest a peak slip of 1.3 m at a depth of 9.6 km for 28 J (Fig. 4), with a northward motion of the hanging wall with respect to the footwall. For the 5 A event, the maximum displacement on the rupture plane is 2.2 m at a depth of 13.6 km; the slip distribution in 19 A is characterized by a single asperity with the maximum slip reaching 2.5 m, located at a depth of 22.2 km. The slip for 5 A and 19 A has a predominant reverse direction with a small right lateral component at depths ranging from 7 to 18 km and 15 to 30 km, respectively (Fig. 4). These estimated centers of the high rupture areas

for each main event are consistent with the centroid solution derived from the GCMT catalog (Fig. S4; Table S4). The estimated strike and location of the source faults imply that the three fault segments may belong to a single fault with irregular geometry, located at the north offshore of Lombok Island, which could be the Flores thrust itself, extending beneath the Sunda volcano arc (Lythgoe et al., 2021; Salman et al., 2020). However, the different dip angles and depths of these three segments also indicate that they may be staggered, suggesting the possibility of the cascading rupture on subparallel splay faults above the Flores thrust (Wang et al., 2020; Yang et al., 2020).

#### 4. Analysis of relocated aftershocks

##### 4.1. Aftershock clustering

Fault orientation can often be constrained by the spatial distribution of numerous early aftershocks if their hypocentre locations are accurate enough (Kato et al., 2006). Therefore, a number of previous studies utilized the distribution of the aftershocks to estimate the orientation of the mainshock rupture plane, e.g., the Mw 6.3 Movri Mountain strike-slip earthquake, 8 June 2003 (Galović et al., 2009) and Mw 6.4

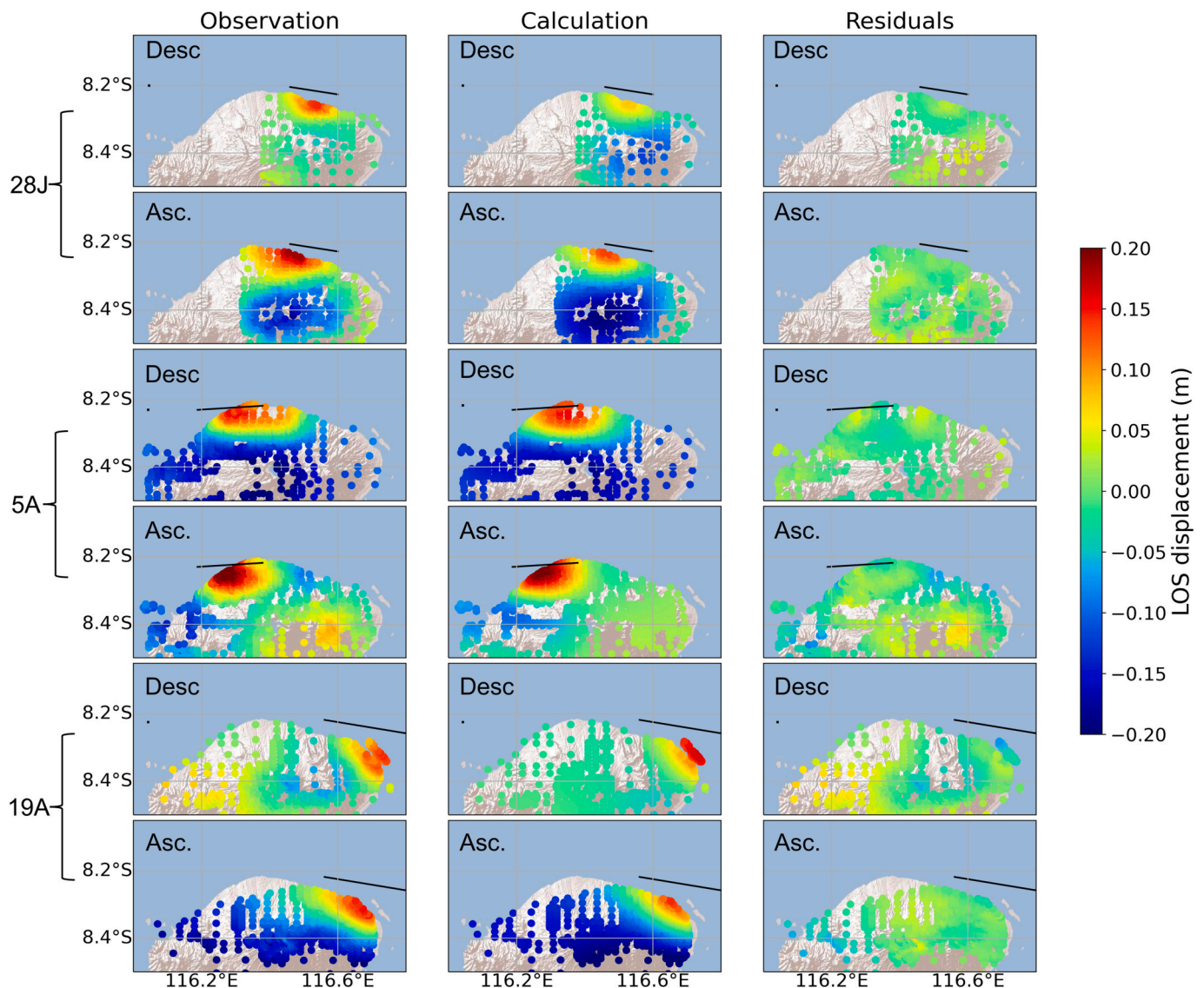
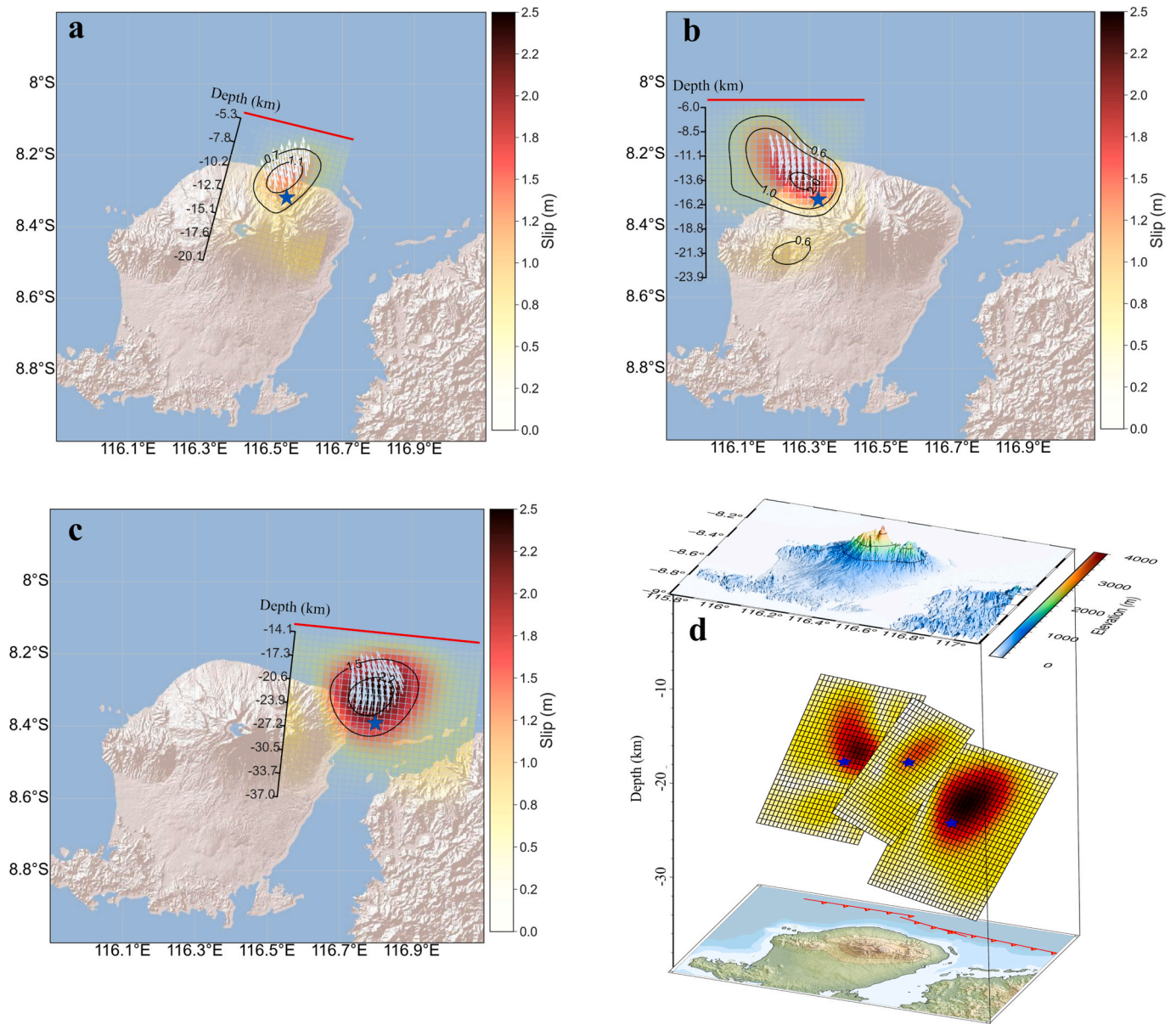


Fig. 3. Calculated LOS displacement based on the layered slip distribution model for events 28 J, 5 A and 19 A respectively and their corresponding residuals. The solid lines represent the vertically projected upper fault edge.



**Fig. 4.** a-c) Slip distribution model for 28 J, 5 A and 19 A, respectively. The white arrows represent the slip direction on the rupture plane. The blue star represents the GCMT centroid location of the three events. The red solid line represents the upper boundary of the estimated rupture plane. d) 3D view of the slip distribution model. The GCMT centroid locations are vertically projected onto the estimated rupture plane; the detailed depths for the centroids and the estimated maximum slip distribution are shown in Table S4. The comparison between the slip distribution and aftershocks is shown in Fig. 6.

Niigata prefecture reverse earthquake, 23 October 2004 (Kato et al., 2006). Theoretically, aftershocks are least abundant in the maximum slip region, which is because the centroid part of the fault rupture has already released most of the energy during the earthquake, therefore there is less potential energy at that location to generate many aftershocks (Galović et al., 2009). For the 2018 Lombok sequence, most of the aftershocks are very shallow, which means their hypocentres are difficult to accurately estimate using low-frequency waveforms. Hence, we analyzed the 130 teleseismic double-difference relocations of aftershocks (based on records from 28 July to 4 August) from Supendi et al. (2020) and 3084 local array double-difference relocation of aftershocks based on records from 5 August to 9 September from Samsi et al. (2020) by comparing their distributions with our estimated rupture planes.

In this study, the three major events of the 2018 Lombok earthquake sequence occurred within only one month, and the estimated rupture areas are spatially close to each other, so it is difficult to separate one earthquake's aftershock sequence from another's. We applied an

unsupervised learning algorithm (ST-DBSCAN) based on Birant and Kut (2007) to classify the Samsi et al. (2020) aftershocks on the similarity of their spatiotemporal attributes, including longitude, latitude, depth and origin time. The algorithm was implemented with three parameters to control the density threshold; two epsilon parameters ( $\epsilon_1$  and  $\epsilon_2$ ) representing the spatial (location) and temporal (origin time) attributes respectively, controlling the maximum acceptable distance; the Minimum Points (MinPts) depended on the size of the seismicity catalog, defining the minimum number of neighbouring items. The K-Nearest Neighbours (KNN) method (Ester et al., 1996) was used to determine the parameters (Birant and Kut, 2007). We used the modified Omori-Utsu Law (Utsu and Ogata, 1995), which describes the occurrence rate of aftershocks  $n(t)$ , to test our clustering results:

$$n(t) = \frac{A}{(c+t)^p} \quad (1)$$

where  $t$  represents the elapsed time since the main shock, while  $A$ ,  $c$  and  $p$  are parameters to be estimated. The decay exponent  $p$  typically falls in the range of 0.5–1.5, and (1) has been used to study spatiotemporal aftershock clustering in different tectonic environments (Utsu and Ogata, 1995). Our clustering results were obtained for  $\mathcal{E}_1 = 0.46$ ,  $\mathcal{E}_2 = 0.45$ , and  $\text{MinPts} = 27$ , which classify the aftershocks that occurred between Aug 5 and Sep 9 into three major clusters, representing the aftershock sequences that followed each of the three main events, and the remaining, unclustered events (Fig. 5a). The identified clusters extracted from the analysis exhibit a typical aftershock decay behavior that follows the Omori-Utsu Law reasonably well (Fig. 5b). The 5 A and 19 A clusters fit the modified Omori–Utsu law, with estimated  $p$ -values of 1.32 and 0.76, respectively (Fig. 5b); the 28 J cluster consists of the Supendi et al. (2020) catalog for the period between 28 J and 5 A, and the clustered results of the Sasmi et al. (2020) catalog with an estimated  $p$ -value of 0.51. Thus, all three identified aftershock clusters have  $p$ -values which fall within the expected range (0.5–1.5). On the one hand, the fact that the three aftershock clusters each have a pattern of temporal decay that follows the Omori-Utsu Law suggests that the

clustering algorithm has effectively separated the aftershock distribution into sequences associated with each mainshock. On the other hand, the algorithm failed to assign 38% of the aftershocks to any cluster. Although these unclustered events could potentially be interpreted using finer clustering by adjusting the clustering parameters ( $\mathcal{E}$  and  $\text{MinPts}$ ), we believe that these events are either (1) associated with one of the three mainshocks, but their location errors are simply too large for the clustering algorithm to do so, or (2) they are related to large aftershocks that occurred following the mainshocks.

#### 4.2. Coulomb failure stress changes

Coulomb stress theory describes the way in which fault friction, pore pressure and stress govern the frictional instability of a fault. Since an earthquake changes the stress field near the fault that ruptures, it also perturbs the Coulomb stress on nearby faults in a way that will either promote or inhibit rupture (reflected as a positive or negative change in Coulomb stress respectively). A common interpretation of the correlation between the distribution of aftershocks and Coulomb failure stress

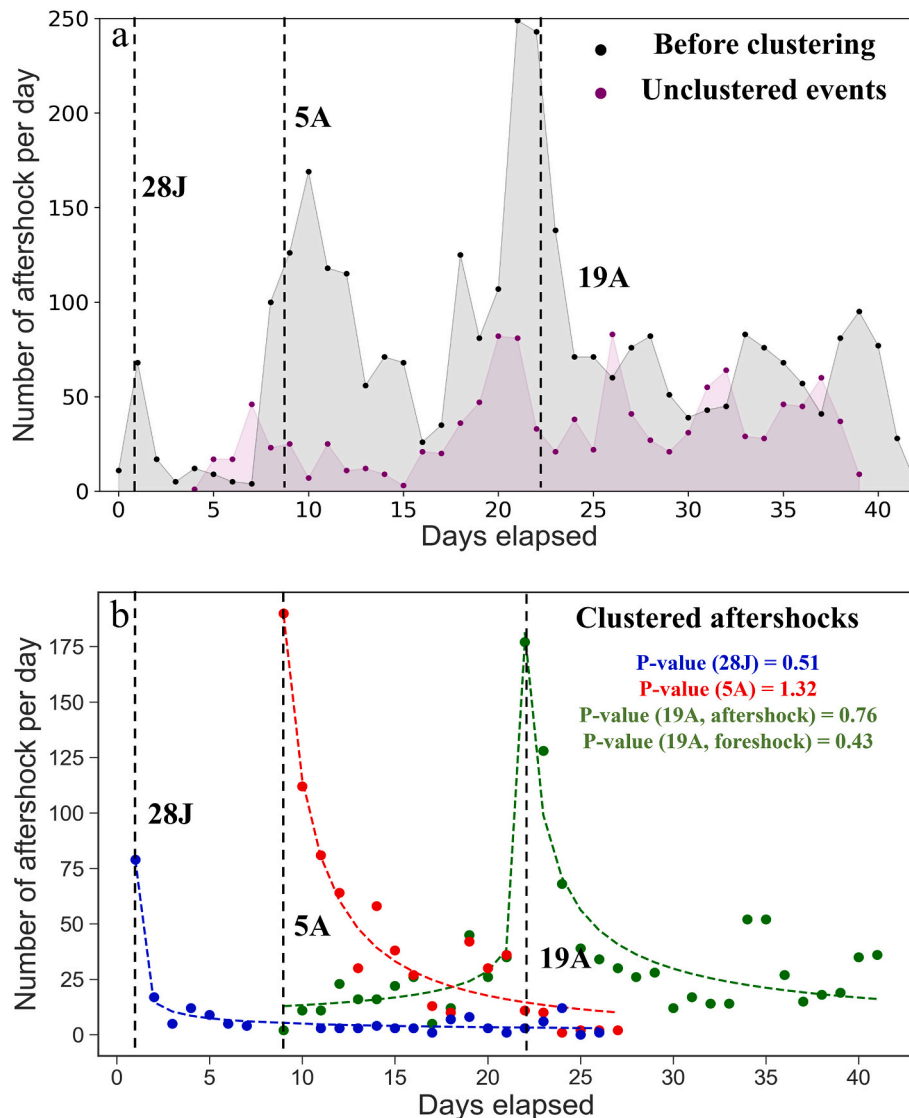


**Fig. 5.** a) The decay in aftershock frequency as a function of time before (grey colour) and after (purple colour) the clustering; the aftershocks are from the Sasmi et al. (2020) catalog. b) Daily number of the clustered aftershocks as a function of the time and the fit to the modified Omori-Utsu law, respectively. The black dashed lines represent the moment that corresponds to the origin time of the three mainshocks, and the dots and dashed lines represent the aftershock clusters and modeled decay following them (blue for 28 J, red for 5 A and green for 19 A). For 28 J, the observations also include the Supendi et al. (2020) catalog for the period between 28 July and 5 August. (For interpretation of the references to colour in this figure legend, the reader is referred to the web version of this article.)

change is that aftershocks tend to fall preferentially in areas where faults have experienced a positive Coulomb stress change as a result of the mainshock rupture (Lin and Stein, 2004). Hence, we compare the clustered aftershocks with the calculated Coulomb stress change for further analysis. The Coulomb stress changes induced by the 2018 Lombok earthquake sequence are calculated based on our estimated co-seismic slip distribution model using Coulomb 3.3 (Toda et al., 2011). We apply the friction coefficient  $\mu = 0.8$  for the calculation, which is suitable for thrust faults (Lin and Stein, 2004). Our results in Fig. 6 illustrate that the Coulomb stress was increased (up to  $\sim 0.5$  Mpa) towards failure on optimally oriented faults in a large part of their immediate vicinity, triggering abundant off-fault aftershocks, which is consistent with the Coulomb stress change pattern of blind thrust faults mentioned in Lin and Stein (2004). The two cross-sections in Fig. 6a pass through the areas containing both clustered aftershocks and non-clustered earthquake activity. Our clustered aftershocks show high spatial correlations with the calculated Coulomb stress change (Fig. 6c-6f). Nearly all the clustered off-fault aftershocks appear to fall in the Coulomb stress increase regions, while for the unclustered events, the numbers of earthquakes are distributed irregularly in the regions of Coulomb stress decrease (Fig. 6c-6f). The cross-sections in Fig. 6b pass through three areas where most clustered aftershocks are concentrated; aftershocks of the 28 J, 5 A and 19 A are mostly distributed in the areas with increased Coulomb stress (Fig. 6g-6i), and less abundant in the high slip patches on the three rupture planes (Fig. 6b), suggesting that the aftershocks are strongly related to increased stress around the main shock rupture areas, which is consistent with our co-seismic slip model.

## 5. Post-seismic deformation

### 5.1. InSAR time series analysis

In order to characterize the post-seismic behavior and the rheological properties that control it, we analyzed the InSAR interferograms using the InSAR time series analysis package LiCSBAS (Morishita et al., 2020) for the first two years after event 19 A. LiCSBAS is based on the New Small Baseline Subset (NSBAS) technique (López-Quiroz et al., 2009), integrated with the LiCSAR products (multi-looked, spatially filtered interferograms), which shortens the time that is spent on Single Look Complex (SLC) data processing (Morishita et al., 2020).

In this study, 337 descending (spanning from 23 August 2018 to 25 July 2020) and 177 ascending (spanning from 20 August 2018 to 28 July 2020) Sentinel-1 acquisitions are used to build up the time series of post-seismic deformation. The spatial and temporal baselines are shorter than 200 m and 36 days respectively, which follows the  $3\bar{\Delta t}$  (where  $\bar{\Delta t}$  is the average temporal sampling interval) rules suggested by Morishita et al. (2020). GACOS corrections are applied to each interferogram to reduce the tropospheric delay. In order to mitigate the influence of cumulative unwrapping errors that occurred during the time series process, we evaluate interferograms by using the loop phase closure method (Biggs et al., 2007). The interferograms are removed when the calculated Root Mean Square (RMS) values of the loop phases are larger than 1.5 rad (Morishita et al., 2020). This left a total of 291 descending and 120 ascending small baseline interferograms used for generating the time series network and conducting the afterslip analysis and viscoelastic modeling. The observed cumulative displacements were computed at five epochs, corresponding to 31 days, 91 days, 181 days, 367 days and 703 days for the descending and 37 days, 97 days, 193 days, 373 days and 709 days for the ascending network, with reference to the first acquisition of 23/08/2018 and 20/08/2018, respectively (Fig. 7).

Our post-seismic time-dependent displacements reveal localized deformation, with increases of the LOS displacement mainly concentrated at the north and east coast of Lombok Island, adjacent to the inferred co-seismic fault trace in the hanging wall side and the Rinjani caldera region (Fig. 7; Fig. S5). The maximum magnitude is around 6 cm

(descending) and 10 cm (ascending) in the east coast region (Fig. 7). The InSAR cumulative LOS displacement time series of the representative areas A (north coast) and B (east coast) show similar trends of linearly increasing LOS. In the denser descending time series, we can observe that two decreases occurred in Oct 2018 and Oct 2019 on the east coast respectively, and back to the previous level in Mar 2019 and Mar 2020, which is coincident with the period of the rainy season (from October to March) on Lombok Island (Idris et al., 2010; Fig. S5). The inflation of the eastern volcano crater region occurred in the first six months after event 19 A, with a magnitude of up to 3 cm (Fig. 7). However, the volcano edifice displays a deflation except in the crater area. Based on the time series plot for the eastern caldera proximity area C, an apparent overall deflation trend can be observed from Sep 2018 to Apr 2020, and subsequently inflation (Fig. S5), which is consistent with the inflation-eruption-deflation pattern suggested in Chaussard et al. (2013). This deformation change may reflect pressure changes in the magma plumbing system caused by the earthquake sequence – i.e., inflation in the first 6 months at the crater area due to an increase in pressure caused by the cumulative co-seismic stress change. However, the total pressure is still below the eruption threshold, and the deflation in response to post-seismic deformation reflects a decrease in the magma system pressure until this is reversed by a long-term increase in pressure since April 2020, possibly due to the gradual influx of new magma (Chaussard et al., 2013). The Standard Deviation (STD) of the InSAR-derived velocity was calculated using the percentile bootstrap method (Morishita et al., 2020), reflecting the uncertainty of the estimated velocity (Fig. S6).

### 5.2. Time-dependent afterslip and viscoelastic relaxation modeling

The long-term and spatially extended post-seismic deformation is assumed to be due to two main mechanisms: afterslip (aseismic slip subsequent to co-seismic slip) which often occurs along a fault surrounding the co-seismic slip area, and viscoelastic relaxation, which is generally believed to occur in the lower crust and upper mantle (e.g., Bürgmann and Dresen, 2008; Diao et al., 2014). Both afterslip and viscoelastic relaxation can relieve parts of the co-seismic stress changes (Bürgmann and Dresen, 2008), and contribute to the near-field and far-field post-seismic deformation, respectively (Bie et al., 2014). Sun and Wang (2015) recognized that for large ( $M_w \geq 7.5$ ) subduction zone megathrust earthquakes, both mechanisms produce similar patterns of surface displacement and therefore cannot be estimated independently; viscous relaxation must be accounted for in order to obtain unbiased estimates of afterslip. However, Sun and Wang (2015) show that for megathrust earthquakes with  $M_w < 7.5$ , the viscoelastic effects are not large enough to bias estimates of afterslip and can be ignored.

Here we consider the hypothesis that, for earthquakes like the 2018 Lombok sequence that occur in a back-arc setting proximate to active volcanism where elevated temperatures may affect rupture on back-arc thrusts (Lythgoe et al., 2021), viscoelastic effects may be important enough to bias estimates of afterslip even for smaller earthquakes. Based on the time-dependent post-seismic dislocation, we can estimate the amount and location of the afterslip with time, and model the rheological properties of the structures beneath the seismogenic zones (Bürgmann and Dresen, 2008; Diao et al., 2014). In this study, we analyze the spatial and temporal distribution of the post-seismic displacement by simulating the time-dependent combined model considering both afterslip and viscoelastic relaxation mechanisms, and investigate the contribution of each mechanism by comparing an afterslip-only model with the simultaneously estimated combined model.

As afterslip often occurs along the mainshock fault but surrounding the main shock rupture area, we extended the co-seismic fault surface of each event along both strike and dip directions. The fault geometry is based on our estimated co-seismic rupture model. We used the SDM technique to estimate the afterslip distribution, as has been done in

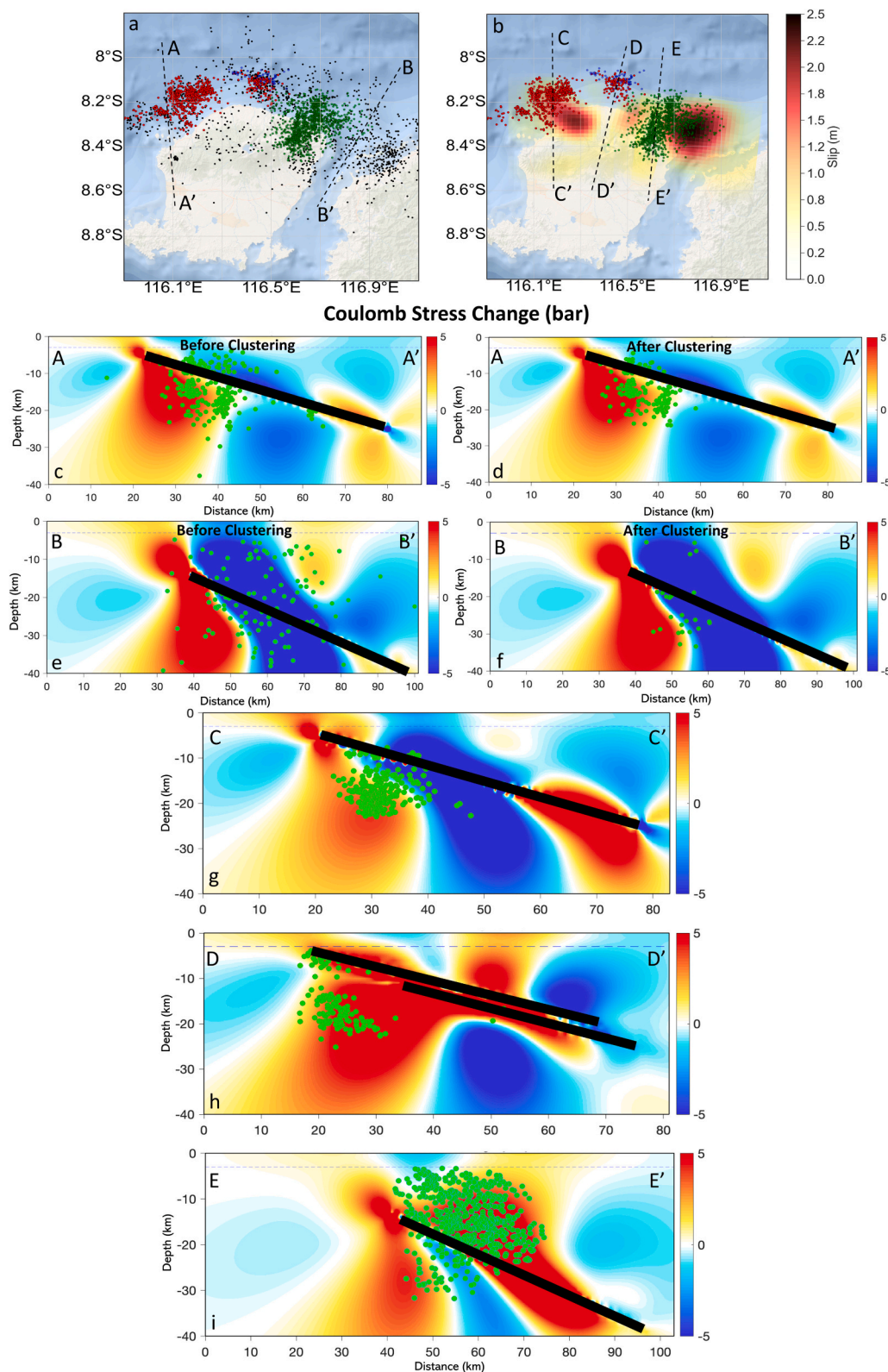


**Fig. 6.** Coulomb stress changes and clustered seismicity associated with the 2018 Lombok earthquake sequence. a) ST-DBSCAN clustering results for the relocated aftershocks. Three major clusters (represented by the blue, red and green dots) are identified, representing the aftershocks following the main events 28 J, 5 A and 19 A, respectively; black dots denote unclustered events. Two profiles (AA' and BB') pass through the areas containing both large amounts of clustered and unclustered seismicity. b) Estimated slip distribution result with the clustered seismicity. Three profiles (CC', DD' and EE') pass through the areas where clustered aftershocks are concentrated. c-i) Vertical cross-section views of the distribution of the Coulomb stress changes, along the profiles shown in Fig. 6a and Fig. 6b; (c) and (e) show the original relocated aftershocks, while the seismicity in (d), (f), and (g-i) are only the clustered aftershocks. Black solid lines represent the fault planes. (For interpretation of the references to colour in this figure legend, the reader is referred to the web version of this article.)

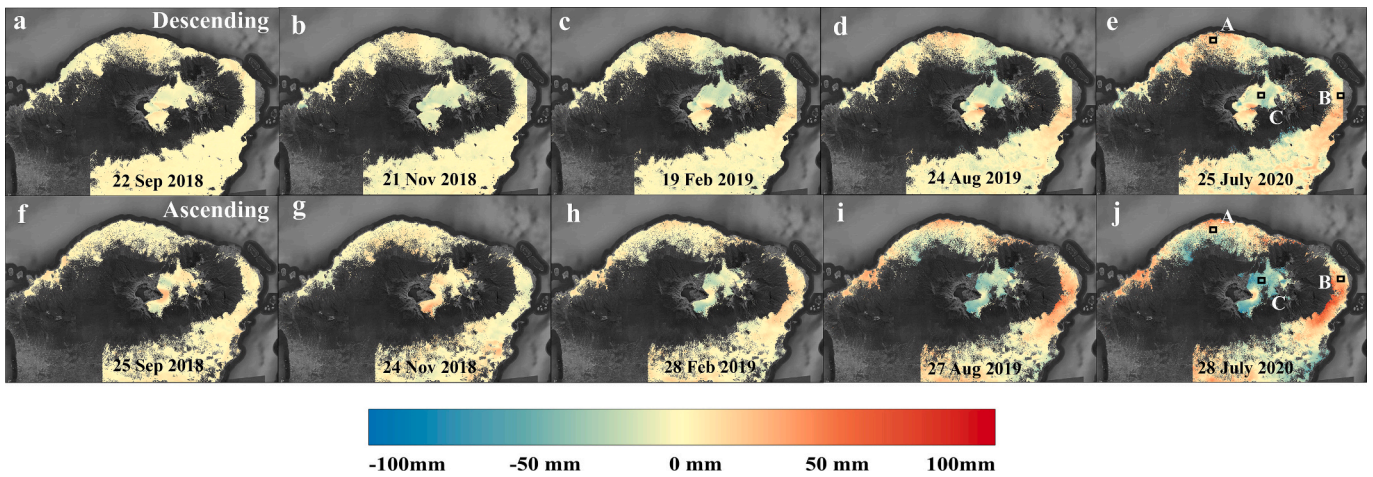


**Fig. 7.** Time-dependent post-seismic deformation following the 2018 Lombok earthquake sequence determined from the Sentinel-1 SAR measurements. (a-e; f-g) The cumulative LOS displacement in descending and ascending track with respect to the date 23 and 20 Aug 2022, respectively. Positive and negative range change is defined as the motion towards and away from the satellite, respectively. The time series of representative areas (black rectangles) are shown in Fig. S5.

previous studies (e.g., Diao et al., 2014; Liu et al., 2016). For the viscoelastic relaxation, we compute co- and post-seismic surface displacement results by using the PSGRN/PSCMP code in Wang et al. (2006), which is based on the viscoelastic-gravitational dislocation theory. We build a three-layer viscoelastic earth model to test the possible viscosities, including an elastic upper crust with a thickness fixed to 20 km, a viscoelastic lower crust (fixed at a depth of 20–30 km) and a viscoelastic asthenosphere (fixed at a depth 30–100 km) corresponding to low-velocity and high-velocity zones, respectively, with the viscosities as free parameters ( $\eta_1$  and  $\eta_2$  respectively) varying over the range from  $1 \times 10^{17}$  to  $1 \times 10^{21}$  Pa s (Fig. 8). For all the layers, a Maxwell rheology is used, which has been widely applied in earthquake models (e.g., Bie et al., 2014; Diao et al., 2014; Liu et al., 2016), and the crust structure and elastic parameters are based on the 1D local velocity model (Table S5) from Sasmi et al. (2020) and formularized in the Nafe-Drake curve from Brocher (2005).

A combined model using both afterslip and viscoelastic relaxation has been used in many studies (e.g., Diao et al., 2014; Liu et al., 2016). However, the best approach for the combined modeling is still under debate. Some previous studies only considered the viscoelastic relaxation caused by the co-seismic slip (e.g., Bie et al., 2014). Diao et al.

(2014) used time-dependent afterslip-only as the driving force of the post-seismic derived viscoelastic relaxation, estimating the two mechanisms in sequential order. However, this method neglects the interaction between the afterslip and viscoelastic relaxation processes (Liu et al., 2016). In order to improve the accuracy of the combined model, we refer to the method in Liu et al. (2016), which allows us to estimate the afterslip and viscoelastic relaxation simultaneously. For each given pair of  $\eta_1$  and  $\eta_2$  values, we simulate the viscoelastic post-seismic deformation at different time epochs ( $i$ ;  $i = 1, 2, 3, \dots$ ), and subtract it from the observed deformation at the corresponding time epoch  $i$ ; this residual deformation is then used to estimate the cumulative afterslip at epoch time  $i$ . The modeled afterslip and co-seismic slip are then combined to drive the viscoelastic post-seismic deformation at the next time epoch  $i + 1$ . In this way, we not only consider the secondary viscoelastic relaxation caused by the afterslip, but also consider the effect of the constantly changed viscoelastic relaxation on the afterslip distribution during the modeling.

We apply a grid search method to find the best-fit viscoelastic parameters (viscosities) and afterslip time series, which minimize the Root Mean Square (RMS) misfit error between our combined models and the observations (Diao et al., 2014; Liu et al., 2016). We set the search

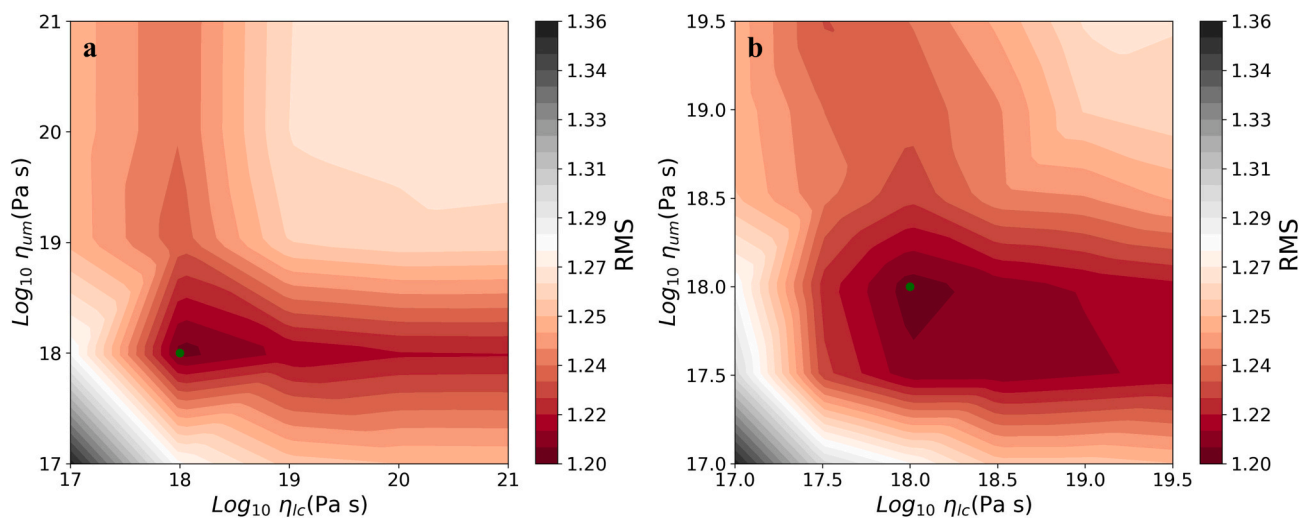


**Fig. 8.** Misfit contour plot in searching the best-fit viscosities for the lower crust (x-axis) and asthenosphere (y-axis). The searching interval in (a) is 1 Pa s of the log viscosity, and in (b) is 0.5 Pa s of the log viscosity. Green points locate the minimum RMS values. (For interpretation of the references to colour in this figure legend, the reader is referred to the web version of this article.)

interval of the viscosity logarithm as 1 unit, searching from  $1 \times 10^{17}$  and  $1 \times 10^{21}$  Pa s for  $\eta_1$  and  $\eta_2$ , and then decreasing the interval to 0.5 unit, narrowing down the searching range to  $1 \times 10^{17}$ – $5 \times 10^{19}$  Pa s (Fig. 8). The best-fit viscosities we obtained from the grid search in our combined model are  $1 \times 10^{18}$  Pa s for both  $\eta_1$  and  $\eta_2$ . The contour plot of the RMS in the  $\eta_1$ - $\eta_2$  plane reveals that the viscosity estimates of the lower crust and asthenosphere have a misfit value of 1.2 cm, suggesting a reasonable viscosity range of  $8.0 \times 10^{17}$ – $1.8 \times 10^{18}$  Pa s for  $\eta_1$  and  $5.0 \times 10^{17}$ – $1.3 \times 10^{18}$  Pa s for  $\eta_2$  (Fig. 8). Based on our optimal viscosity estimates, we calculate the cumulative post-seismic afterslip in the combined model at four epochs every six months until two years after the 19 A mainshock. The spatial and temporal distribution of the afterslip derived from the combined model is shown in Fig. 9, indicating three localized high-slip patches. The two separate afterslip zones on the 5 A rupture plane are distributed at the downdip and up-dip areas of the maximum co-seismic rupture regions, respectively, with the maximum afterslip of  $\sim 0.5$  m two years after the mainshock, while the afterslip pattern on the 19 A rupture plane is reflected as one single major asperity with a maximum afterslip displacement of  $\sim 0.7$  m (Fig. 9). This kind of long-term afterslip may occur on a dominantly creeping fault or in a geological regime of bedrock faulting (Lienkaemper and McFarland, 2017). The checkerboard tests in previous studies suggest an acceptable fault slip resolution for the InSAR-derived source fault model (e.g., Lythgoe et al., 2021; Salman et al., 2020; Wang et al., 2020). Salman et al. (2020) tested the slip resolution by using a synthetic input slip range from 0 to 100 cm, and suggested that the poor resolution is mainly concentrated at the latitude from  $7.9^\circ$  S to  $8.1^\circ$  S due to the lack of offshore deformation signal, whereas for the latitude range from  $8.1^\circ$  S to  $8.6^\circ$  S (where our estimated afterslip occurs), the inverted slip has a good resolution.

The upper afterslip patch on the 5 A fault plane and the major slip patch on the 19 A fault plane have not shown significant spatial migration over the timespan of our model, whereas the deep afterslip patch on the 5 A rupture plane consists of two small-scale high-slip patches which were gradually merged at least by six months after the mainshock (Fig. 9). For all the high-slip zones, the post-seismic afterslip

is generally characterized by a higher increase rate during the first year after the mainshock, and exponentially decaying in the subsequent periods (Fig. S7). We also simulate the time-dependent cumulative post-seismic deformation by only considering the mechanism of afterslip for the same time interval (Fig. S8). The discrepancy between the time-dependent combined model and the afterslip-only model reveals the effect of the viscoelastic relaxation in different epochs. In both models, the spatial distribution of the estimated afterslip is stable in different epochs. The comparison between the combined and afterslip-only models is discussed in the next section.

## 6. Co-seismic and post-seismic fault slip

Our co-seismic slip distribution model for the 2018 Lombok earthquake sequence illustrates three isolated high-slip zones with a slip displacement  $>1$  m and several medium-slip zones with a slip displacement  $\sim 0.6$  m (Fig. 4). The fault geometries we estimated by inverting the InSAR dataset using rectangular dislocations embedded in a homogeneous elastic half-space are consistent with the solutions based on the multi-layered half-space in Salman et al. (2020). However, comparing with studies that assumed a homogenous half-space for the slip distribution modeling (e.g., Salman et al., 2020; Wang et al., 2020), our solutions are more consistent with Lythgoe et al. (2021), who also detected multiple smaller slip asperities for 5 A and a single major asperity for 19 A by assuming a layered crust. The Coulomb stress changes induced by the 28 J event caused positive Coulomb stress changes of over 0.5 Mpa at the hypocenter location as well as the east major slip area of the 5 A event, which indicates that the 28 J event promoted the occurrence of the 5 A event (Fig. S10). For the 19 A event, the 28 J event has released  $\sim 0.02$  Mpa Coulomb stress that surrounds the west rupture area of the 19 A. However, the subsequent 5 A event increases the Coulomb stress to  $\sim 0.01$  Mpa for the same area (Fig. S10). Thus, the case is less strong that the Coulomb stress changes due to events 5 A and 28 J were large enough to trigger event 19 A.

The mainshock also alters the stress field near the mainshock rupture

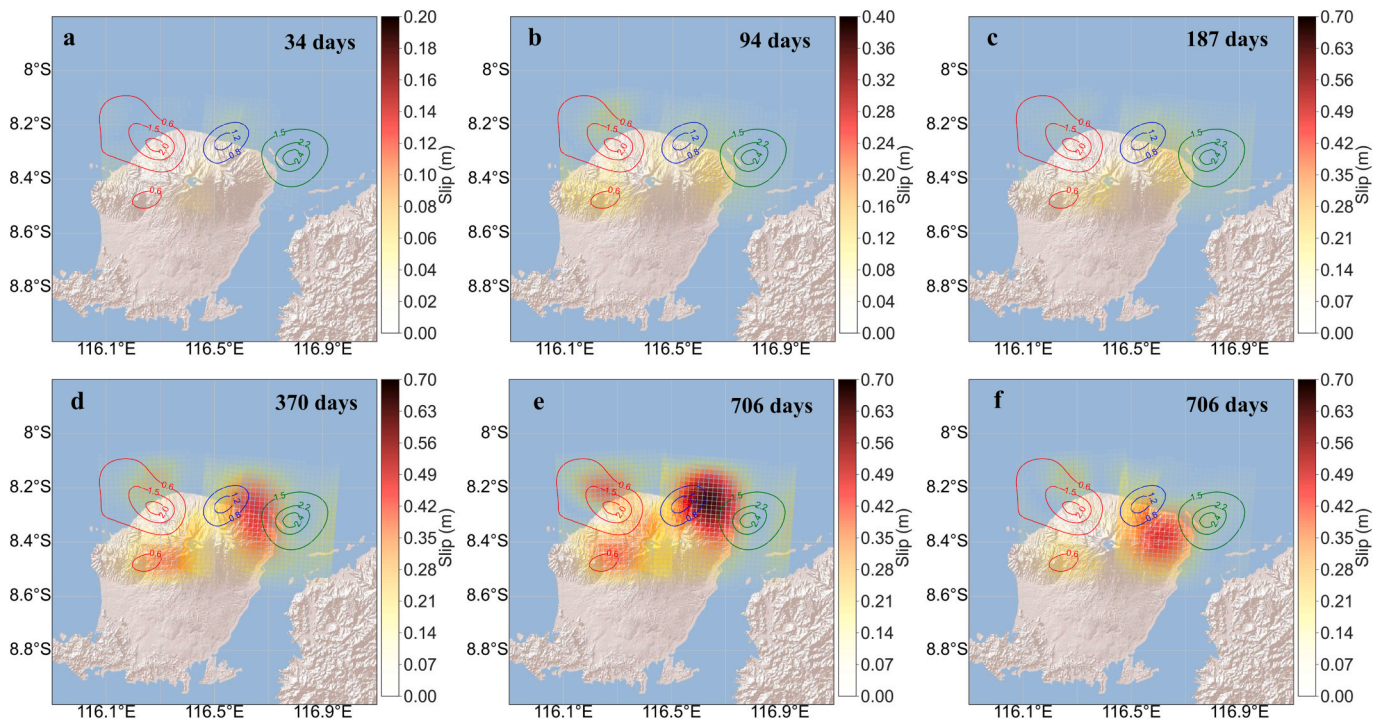


**Fig. 9.** a-e) Time-dependent afterslip distribution derived from the combined model considering both afterslip and viscoelastic relaxation mechanisms. Note that plots (a) and (b) have different colour scales. The red, blue and green contours represent the estimated co-seismic slip distribution of 28 J, 5 A, and 19 A, respectively. f) Afterslip distribution in 706 days following the 19 A event using the afterslip-only model. The residuals of both types of models are shown in Fig. S9.

areas, resulting in large positive Coulomb stress changes on nearby optimally oriented faults that promote the occurrence of aftershocks for several weeks following the mainshock occurrence (Fig. 6). These aftershocks cluster in areas surrounding the main asperities, a pattern observed in many mainshock-aftershock sequences (e.g., Gallovič et al., 2009).

The co-seismic stress changes caused by the mainshock ruptures also resolve to positive Coulomb stress changes along the mainshock fault planes, in the same areas around the main asperities where aftershocks cluster, and this appears to promote the progression of afterslip in these areas (Fig. 6; Fig. 9). Previous studies have observed the simultaneous progression of afterslip with the spread of aftershocks along the fault plane and interpreted this as implying that afterslip drives the aftershock occurrence (Perfettini et al., 2018). What we observe in the Lombok earthquake sequence is that, while both afterslip and aftershocks occur in the same areas of positive Coulomb stress change, the aftershocks decay rapidly, in a matter of weeks, while the afterslip develops over an interval of two years (Fig. 9; Table S6). Since the aftershocks require brittle, i.e., velocity weakening, frictional fault behavior while afterslip implies velocity strengthening behavior, we tentatively conclude that most if not all of the aftershocks are occurring in the brittle material surrounding but not on the fault plane, while the afterslip may be occurring in a zone of fault gouge along the up-dip part of the fault plane that exhibits velocity strengthening behavior (Marone et al., 1991).

The results of our approach for estimating afterslip while also accounting for viscoelastic deformation are in accord with those of Sun and Wang (2015) who found that approaches that ignore viscoelastic deformation will overestimate afterslip down-dip of the rupture zone, and underestimate afterslip up-dip of the rupture zone. This is exactly the behavior we observe in Fig. 9. (see also Fig. S8), where we compare the “combined” relaxation + afterslip model with an afterslip-only (i.e., no viscoelastic relaxation) model. As discussed in Sun and Wang (2015), this occurs because afterslip and relaxation result in codirectional surface motion above the down-dip limit of rupture, but opposing surface motion above the up-dip limit. As predicted by Sun and Wang (2015), the difference in estimated afterslip can be substantial, where Table S6 shows the afterslip-only model underestimates the maximum up-dip afterslip for event 5 A (19 A) as 22.4 (47.0) cm, whereas the combined model estimates 39.0 (65.4) cm, a difference of 42 (28)%.

While the way in which viscoelastic relaxation influences our estimates of afterslip agrees with the results of Sun and Wang (2015), the magnitude of the viscoelastic effect appears to be much larger than they describe for earthquakes of this size. Sun and Wang (2015) assert that viscoelastic effects are negligible for earthquakes having  $M_W < 7.5$ , but we find they are worth considering at least for events 5 A and 19 A, with  $M_W$  of 7.0. We ascribe this discrepancy to the subduction zone setting considered by Sun and Wang (2015), involving an upper plate with an elastic crust of 30 km thickness. The 2018 Lombok earthquakes instead occurred in a back-arc setting, very close to an active volcano. Such back-arc regions are often characterized by a lower crust having low viscosity, due to temperatures that can be much higher than typical continental crust (Hyndman, 2019). Hyndman (2019) describes how such “hot” back-arcs can have temperature gradients twice as high as those of stable continental areas, resulting in Moho temperatures  $>800$  °C. Based on an analysis of Lombok seismicity, Lythgoe et al. (2021) suggest that the temperature gradient beneath Rinjani might be as high as 48°/km, compared to an estimated regional temperature gradient of 18 °C. Although our estimate of a lower crustal viscosity of  $1 \times 10^{18}$  Pa s might seem low compared to typical lower continental crust (Shinevar et al., 2015), it is similar to the lower crust of other hot back-arcs Hyndman (2019). We believe this low viscosity of the lower crust leads to an enhanced post-seismic viscous relaxation that is important to account for in estimates of afterslip following the 2018 Lombok earthquakes.

The Root Mean Square (RMS) misfits for the combined model and afterslip-only model are 0.016 m and 0.020 m, respectively. However,

the reduced RMS of the combined model may simply reflect the increased model complexity, and it is not clear whether this complexity is justified by the reduced misfit. The “thermal squeezing” of the seismogenic zone proposed by Lythgoe et al. (2021) suggests that the lower crust near Rinjani is better characterized by low viscosity, in agreement with our combined “viscoelastic relaxation + afterslip” model; however, it is unclear how far this low viscosity extends beyond the vicinity of Rinjani. We prefer to regard the two models as end members of a range of models that can fit the InSAR data, so that the true afterslip lies somewhere between the combined and pure afterslip models.

## 7. Conclusion

The study of the 2018 Lombok earthquake sequence is of great research value due to the interaction between the active Flores back-arc thrust and the Rinjani volcano. This study investigates both co- and post-seismic rupture processes for the 2018 Lombok earthquake sequence, which comprised a series of spatiotemporally close earthquakes. We perform a comprehensive analysis of time-dependent co- and post-seismic slip, the associated Coulomb failure stress changes, and clustered relocated aftershocks based on an unsupervised learning algorithm, whose estimates indicate a high consistency among each other.

We use 337 descending and 177 ascending acquisitions measured in the two years after the main event to perform a time series analysis for the post-seismic mechanisms including afterslip and viscoelastic relaxation. We compare the time-dependent afterslip-only and combined afterslip/relaxation models. Although previous studies have suggested the effect of viscoelastic relaxation on aftershock determination should be very small for earthquakes smaller than magnitude 7.5 (Sun and Wang, 2015), we found that the discrepancy in the afterslip estimated using the two types of models can reach over 40%, and the spatial distribution of the high afterslip is also located at different areas in these two models, especially for events 5 A and 19 A. This suggests that the viscoelastic relaxation effect in estimating afterslip might be significant for earthquakes as small as magnitude 7.0, if they occur in a back-arc and/or volcanic environment. We think this may be due to the relatively low viscosity of  $1 \times 10^{18}$  Pa s estimated for the lower crust, which is mainly due to the influence of hot back-arc and the active Rinjani volcano (Lythgoe et al., 2021). However, it is difficult to claim the viscoelastic effect is well-resolved, since the afterslip-only model also provides a good fit to the data.

We found that the positive co-seismic changes in Coulomb stress near the mainshock faults correlated well with both aftershock and afterslip occurrence, although the aftershocks decayed in 1–2 weeks whereas the afterslip progressed up-dip over the course of two years. This implies that, at least for the Lombok earthquake sequence, afterslip did not drive aftershock occurrence. Instead, we believe that in the immediate co-seismic period the Coulomb stress change associated with the mainshock promoted brittle failure of faults near but not on the mainshock fault surface. The same Coulomb stress change promotes afterslip occurrence on the main fault surface, but this occurs over a much longer time frame in a zone of velocity-strengthening fault gouge. To the extent that this implies that the mainshocks occurred on a mature fault, this supports the hypothesis of Lythgoe et al. (2021) that the Lombok earthquakes occurred on the irregularly shaped Flores Back-arc thrust itself, rather than on splay faults that branch from it, as has been proposed in other studies (Yang et al., 2020).

## CRedit authorship contribution statement

**Siyuan Zhao:** Writing – review & editing, Writing – original draft, Visualization, Software, Methodology, Investigation, Formal analysis. **Simon McClusky:** Writing – review & editing, Supervision, Investigation, Formal analysis. **Phil R. Cummins:** Writing – review & editing, Supervision, Investigation, Formal analysis. **Meghan S. Miller:** Writing – review & editing, Supervision.

## Declaration of competing interest

The authors declare that they have no known competing financial interests or personal relationships that could have appeared to influence the work reported in this paper.

## Data availability

All Sentinel-1 datasets used for the co-seismic analysis in this study are provided by Alaska Satellite Facility (ASF), which can be found and downloaded via ASF data search vertex (<https://search.asf.alaska.edu/>). The unwrapped interferograms used for the InSAR time series analysis are derived from COMET-LiCS Sentinel-1 InSAR portal (<https://comet.nerc.ac.uk/COMET-LiCS-portal/>) with the frame ID 156A\_09814\_081406 for the ascending track and 032D\_09854\_070505 for the descending track. All the InSAR products and scripts are available from the corresponding author.

## Acknowledgments

The authors thank Alaska Satellite Facility (ASF) and European Space Agency (ESA) for the Sentinel-1 single-look complex data. Additional thanks to NASA for SRTM DEM. Furthermore, we are grateful to Dr. Rongjiang Wang for providing SDM and PSGRN/PSCMP; Sandwell et al. (2011) for providing GMTSAR; Centre for the Observation and Modeling of Earthquakes, Volcanoes and Tectonics (COMET) and Morishita et al. (2020) for the GBIS software package and LiCSAR/LiCSBAS.

## Appendix A. Supplementary data

Supplementary data to this article can be found online at <https://doi.org/10.1016/j.rse.2024.114063>.

## References

- Albino, F., Biggs, J., Yu, C., Li, Z., 2020. Automated methods for detecting volcanic deformation using Sentinel-1 InSAR time series illustrated by the 2017–2018 unrest at Agung, Indonesia. *J. Geophys. Res. Solid Earth* 125 e2019JB017908.
- Bagnardi, M., Hooper, A., 2018. Inversion of surface deformation data for rapid estimates of source parameters and uncertainties: a Bayesian approach. *Geochem. Geophys. Geosyst.* 19, 2194–2211.
- Bie, L., Ryder, I., Nippres, S.E., Bürgmann, R., 2014. Coseismic and post-seismic activity associated with the 2008 M w 6.3 Damxung earthquake, Tibet, constrained by InSAR. *Geophys. J. Int.* 196, 788–803.
- Biggs, J., Wright, T., Lu, Z., Parsons, B., 2007. Multi-interferogram method for measuring interseismic deformation: Denali fault, Alaska. *Geophys. J. Int.* 170, 1165–1179.
- Birant, D., Kut, A., 2007. ST-DBSCAN: an algorithm for clustering spatial-temporal data. *Data Knowl. Eng.* 60, 208–221.
- Brocher, T.M., 2005. Empirical relations between elastic wavespeeds and density in the Earth's crust. *Bull. Seismol. Soc. Am.* 95, 2081–2092.
- Bürgmann, R., Dresen, G., 2008. Rheology of the lower crust and upper mantle: evidence from rock mechanics, geodesy, and field observations. *Annu. Rev. Earth Planet. Sci.* 36, 531–567.
- Cattin, R., Briole, P., Lyon-Caen, H., Bernard, P., Pinettes, P., 1999. Effects of superficial layers on coseismic displacements for a dip-slip fault and geophysical implications. *Geophys. J. Int.* 137, 149–158.
- Chaussard, E., Amelung, F., Aoki, Y., 2013. Characterization of open and closed volcanic systems in Indonesia and Mexico using InSAR time series. *J. Geophys. Res. Solid Earth* 118, 3957–3969.
- Diao, F., Xiong, X., Wang, R., Zheng, Y., Walter, T.R., Weng, H., Li, J., 2014. Overlapping post-seismic deformation processes: Afterslip and viscoelastic relaxation following the 2011 M w 9.0 Tohoku (Japan) earthquake. *Geophys. J. Int.* 196, 218–229.
- Ester, M., Kriegel, H.-P., Sander, J., Xu, X., 1996. A density-based algorithm for discovering clusters in large spatial databases with noise. In: *kdd*, pp. 226–231.
- Foden, J., JD, F., 1981. The Geochemistry and Petrology of the Basalt-Andesite-Dacite Suite from Rinjani Volcano, Lombok: Implications for the Petrogenesis of Island Arc, Calcalkaline Magmas.
- Gabriel, A.K., Goldstein, R.M., Zebker, H.A., 1989. Mapping small elevation changes over large areas: differential radar interferometry. *J. Geophys. Res. Solid Earth* 94, 9183–9191.
- Gallovič, F., Zahradník, J., Krížová, D., Plicka, V., Sokos, E., Serpetsidaki, A., Tselentis, G. A., 2009. From earthquake centroid to spatial-temporal rupture evolution: Mw 6.3 Movri Mountain earthquake, June 8, 2008, Greece. *Geophys. Res. Lett.* 36.
- Hamilton, W.B., 1979. Indonesia. Departemen Pertambangan., & United States. Agency for International Development. In: *Tectonics of the Indonesian Region*. U.S. Govt. Print. Off. Washington.
- Hanifa, R.N., Anantaseña, Y., Sadly, M., Ito, T., 2019. Ground deformation identification related to 2018 Lombok earthquake series based on Sentinel-1 data. In: *IOP Conference Series: Earth and Environmental Science*. IOP Publishing, p. 012004.
- Hanssen, R.F., 2001. *Radar Interferometry: Data Interpretation and Error Analysis*. Springer Science & Business Media.
- Hong, S., Zhou, X., Zhang, K., Meng, G., Dong, Y., Su, X., Zhang, L., Li, S., Ding, K., 2018. Source model and stress disturbance of the 2017 Jiuzhaigou mw 6.5 earthquake constrained by InSAR and GPS measurements. *Remote Sens.* 10, 1400.
- Hyndman, R., 2019. Mountain building orogeny in precollision hot backarcs: north American cordillera, India-Tibet, and Grenville Province. *J. Geophys. Res. Solid Earth* 124, 2057–2079.
- Idris, M.H., Yasin, I., Mahrup, M., Abawi, Y., 2010. Spatial and temporal pattern of rainfall in southern Lombok eastern Indonesia. *J. Penelitan Univer. Mataram* 2, 71–79.
- Jónsson, S., Zebker, H., Segall, P., Amelung, F., 2002. Fault slip distribution of the 1999 M w 7.1 Hector mine, California, earthquake, estimated from satellite radar and GPS measurements. *Bull. Seismol. Soc. Am.* 92, 1377–1389.
- Kato, A., Sakai, S.I., Hirata, N., Kurashimo, E., Iidaka, T., Iwasaki, T., Kanazawa, T., 2006. Imaging the seismic structure and stress field in the source region of the 2004 mid-Niigata prefecture earthquake: structural zones of weakness and seismogenic stress concentration by ductile flow. *J. Geophys. Res. Solid Earth* 111.
- Lienkaemper, J.J., McFarland, F.S., 2017. Long-term afterslip of the 2004 M 6.0 Parkfield, California, earthquake—implications for forecasting amount and duration of afterslip on other major creeping faults. *Bull. Seismol. Soc. Am.* 107, 1082–1093.
- Lin, J., Stein, R.S., 2004. Stress triggering in thrust and subduction earthquakes and stress interaction between the southern San Andreas and nearby thrust and strike-slip faults. *J. Geophys. Res. Solid Earth* 109.
- Liu, Y., Xu, C., Li, Z., Wen, Y., Chen, J., Li, Z., 2016. Time-dependent afterslip of the 2009 mw 6.3 dachaidan earthquake (China) and viscosity beneath the qaidam basin inferred from postseismic deformation observations. *Remote Sens.* 8, 649.
- Lohman, R.B., Simons, M., 2005. Some thoughts on the use of InSAR data to constrain models of surface deformation: noise structure and data downsampling. *Geochem. Geophys. Geosyst.* 6.
- López-Quiroz, P., Doin, M.-P., Tupin, F., Briole, P., Nicolas, J.-M., 2009. Time series analysis of Mexico City subsidence constrained by radar interferometry. *J. Appl. Geophys.* 69, 1–15.
- Lythgoe, K., Muzli, M., Bradley, K., Wang, T., Nugraha, A.D., Zulfakriza, Z., Widiyantoro, S., Wei, S., 2021. Thermal squeezing of the seismogenic zone controlled rupture of the volcano-rooted Flores thrust. *Sci. Adv.* 7, eabe2348.
- Marone, C.J., Scholtz, C., Bilham, R., 1991. On the mechanics of earthquake afterslip. *J. Geophys. Res. Solid Earth* 96, 8441–8452.
- McCaffrey, R., Nábèlek, J., 1984. The geometry of back arc thrusting along the eastern Sunda arc, Indonesia: constraints from earthquake and gravity data. *J. Geophys. Res. Solid Earth* 89, 6171–6179.
- Morishita, Y., Lazecky, M., Wright, T.J., Weiss, J.R., Elliott, J.R., Hooper, A., 2020. LiCSBAS: an open-source InSAR time series analysis package integrated with the LiCSAR automated Sentinel-1 InSAR processor. *Remote Sens.* 12, 424.
- Okada, Y., 1985. Surface deformation due to shear and tensile faults in a half-space. *Bull. Seismol. Soc. Am.* 75, 1135–1154.
- Perfettini, H., Frank, W., Marsan, D., Bouchon, M., 2018. A model of afterslip migration driven by afterslip. *Geophys. Res. Lett.* 45, 2283–2293.
- Pritchard, M., Simons, M., Rosen, P., Hensley, S., Webb, F., 2002. Co-seismic slip from the 1995 July 30 M w = 8.1 Antofagasta, Chile, earthquake as constrained by InSAR and GPS observations. *Geophys. J. Int.* 150, 362–376.
- Salman, R., Lindsey, E.O., Lythgoe, K.H., Bradley, K., Muzli, M., Yun, S.H., Chin, S.T., Tay, J., C.W., Costa, F., Wei, S., 2020. Cascading Partial Rupture of the Flores Thrust during the 2018 Lombok Earthquake Sequence, Indonesia. *Seismological Research Letters*.
- Sandwell, D., Mellors, R., Tong, X., Wei, M., Wessel, P., 2011. *Gmtsar: An InSAR Processing System Based on Generic Mapping Tools*.
- Saputra, A.W.W., Zakaria, N.A., Weng, C.N., 2020. Changes in land use in the Lombok River basin and their impacts on River Basin management sustainability. In: *IOP Conference Series: Earth and Environmental Science*. IOP Publishing, p. 012036.
- Sasmi, A.T., Nugraha, A.D., Muzli, M., Widiyantoro, S., Zulfakriza, Z., Wei, S., Sahara, D. P., Riyanto, A., Puspito, N.T., Priyono, A., 2020. Hypocenter and Magnitude Analysis of Aftershocks of the 2018 Lombok, Indonesia, Earthquakes Using Local Seismographic Networks. *Seismological Research Letters*.
- Shinevar, W.J., Behn, M.D., Hirth, G., 2015. Compositional dependence of lower crustal viscosity. *Geophys. Res. Lett.* 42, 8333–8340.
- Silver, E.A., Reed, D., McCaffrey, R., Joyodiwiryo, Y., 1983. Back arc thrusting in the eastern Sunda arc, Indonesia: a consequence of arc-continent collision. *J. Geophys. Res. Solid Earth* 88, 7429–7448.
- Smittarello, D., Cayol, V., Pinel, V., Froger, J.-L., Peltier, A., Dumont, Q., 2019. Combining InSAR and GNSS to track magma transport at basaltic volcanoes. *Remote Sens.* 11, 2236.
- Sun, T., Wang, K., 2015. Viscoelastic relaxation following subduction earthquakes and its effects on afterslip determination. *J. Geophys. Res. Solid Earth* 120, 1329–1344.
- Supendi, P., Nugraha, A., Widiyantoro, S., Pesicek, J., Thurber, C., Abdullah, C., Daryono, D., Wiyono, S., Shiddiqi, H., Rosalia, S., 2020. Relocated aftershocks and background seismicity in eastern Indonesia shed light on the 2018 Lombok and Palu earthquake sequences. *Geophys. J. Int.* 221, 1845–1855.

- Toda, S., Stein, R.S., Sevilgen, V., Lin, J., 2011. Coulomb 3.3 Graphic-rich deformation and stress-change software for earthquake, tectonic, and volcano research and teaching—user guide. In: US Geological Survey Open-File Report, 1060, p. 63.
- Utsu, T., Ogata, Y., 1995. The centenary of the Omori formula for a decay law of aftershock activity. *J. Phys. Earth* 43, 1–33.
- Wang, R., Martín, F.L., Roth, F., 2003. Computation of deformation induced by earthquakes in a multi-layered elastic crust—FORTRAN programs EDGRN/EDCMP. *Comput. Geosci.* 29, 195–207.
- Wang, R., Lorenzo-Martín, F., Roth, F., 2006. PSGRN/PSCMP—a new code for calculating co-and post-seismic deformation, geoid and gravity changes based on the viscoelastic-gravitational dislocation theory. *Comput. Geosci.* 32, 527–541.
- Wang, R., Diao, F., Hoehner, A., 2013. SDM-A geodetic inversion code incorporating with layered crust structure and curved fault geometry. In: EGU General Assembly Conference Abstracts.
- Wang, C., Wang, X., Xiu, W., Zhang, B., Zhang, G., Liu, P., 2020. Characteristics of the seismogenic faults in the 2018 Lombok, Indonesia, earthquake sequence as revealed by inversion of InSAR measurements. *Seismol. Res. Lett.* 91, 733–744.
- Williams, C.A., Wadge, G., 1998. The effects of topography on magma chamber deformation models: application to Mt. Etna and radar interferometry. *Geophys. Res. Lett.* 25, 1549–1552.
- Yang, X., Singh, S.C., Tripathi, A., 2020. Did the Flores backarc thrust rupture offshore during the 2018 Lombok earthquake sequence in Indonesia? *Geophys. J. Int.* 221, 758–768.
- Yu, C., Li, Z., Penna, N.T., Crippa, P., 2018. Generic atmospheric correction model for interferometric synthetic aperture radar observations. *J. Geophys. Res. Solid Earth* 123, 9202–9222.
- Zhao, S., McClusky, S., Cummins, P.R., Miller, M.S., Nugroho, H., 2023. New insights into crustal deformation of the Indonesia–Australia–New Guinea collision zone from a broad-scale kinematic model. *J. Geophys. Res. Solid Earth* 128 e2022JB024810.